Thomson Scattering Measurements in the Krypton Plume of a Lanthanum Hexaboride Hollow Cathode in a Large Vacuum Test Facility

Jean Luis Suazo Betancourt,[1] Naia Butler-Craig,[1] Julian Lopez-Uricoechea,[1] Junhwi Bak,[2] Dongho Lee,[1] Adam M. Steinberg,[1] and Mitchell L. R. Walker[1]
[1)] *School of Aerospace Engineering, Georgia Institute of Technology, Atlanta, GA 30318*
[2)] *Department of Aerospace Engineering, Texas A&M University, College Station, TX 77843*

(*Electronic mail: jlsb3@gatech.edu)

(Dated: 6 February 2024)

Laser Thomson scattering is a minimally intrusive diagnostic technique for determining electron temperature, density, and bulk velocity in plasma systems. Advances in technology have made possible the application of Thomson scattering to electric propulsion-relevant plasma systems, with reported electron number density detection limits as low as $1{\times}10^{16}\mathrm{m}^{-3}$, and electron temperatures from one-to-tens eV. However, the implementation of laser Thomson scattering in large vacuum testing facilities, wherein electric propulsion (EP) devices are tested, remains a challenge. This work presents the implementation of a laser Thomson scattering system in a large vacuum test facility at the Georgia Tech High Power Electric Propulsion Laboratory. The diagnostic was optimized for maximum light collection efficiency and ease of re-alignment while the facility is at vacuum. The high light-collection efficiency allowed reduced accumulation times to achieve the target detection limit of 1×10^{17} m^{-3}. The diagnostic is used to measure axial electron property profiles in the near-field plume of a lanthanum hexaboride hollow cathode operating at 25 A on krypton at a background pressure of 1.3×10^{-6} Torr-Kr. The diagnostic is quantitatively compared to similar systems in the literature. The resulting axial points, collected from 2 mm to 8 mm downstream of the cathode keeper orifice, are qualitatively and quantitatively compared with simulations and experimental measurements made with electrostatic probes and laser-induced fluorescence. The main quantitative difference between measured values and results is the one to two order of magnitude difference in the peak electron density, being attributed to the relative size and location of the external anode with respect to the cathode keeper.

Keywords: Thomson scattering, Raman scattering, electron velocity distribution functions, statistical inversion, Bayesian model selection, Bayesian inversion, Maxwellian, Druyvesteyn

I. INTRODUCTION

Hall effect thrusters (HETs) are electrostatic devices that leverage a standing axial electric field and standing radial magnetic fields in order to ionize and accelerate neutral propellant gas to create thrust[1]. One of the main goals of the standing magnetic field is to confine electrons that are extracted from a hollow cathode in order to efficiently ionize the neutral propellant gas, as well as to neutralize the thruster plume. The hollow cathode is extremely important to the operation of these thrusters, as it is the main source of electrons for ionization and neutralization[2]. The internal and near-field cathode plasma physics are important to both the performance and lifetime of HETs but, at present, are not fully understood. This highlights the need for measurements investigating key plasma properties in hollow cathodes.

Recently, HETs have had their magnetic field topology designed in such a way as to provide shielding to the inner discharge channel walls, known as magnetic shielding (MS)[3]. MS effectively eliminates the main life-limiting factor in traditionally unshielded HETs, namely discharge channel erosion. With MS extending life for HETs, crewed and uncrewed missions like the Asteroid Retrieval Robotic Mission aim to achieve HET lifetimes exceeding 100 kHrs[4,5]. This necessitates high discharge power single and multi-channel HETs with discharge currents of up to 500 A. The discharge and lifetime requirements of this mission highlight the need for continuous development of high-power HETs and high-current hollow cathodes. Cathode insert, orifice, and keeper geometry, as well as insert material, are key in developing high-current cathodes. Additionally, simulations of the plasma behavior and corroborative measurements of the plasma for simulation validation are critical for high-current hollow cathode and high-power HET development.

Internal and external measurements of hollow cathode operation have focused on stand-alone, in-thruster simulating, and in-thruster operation in diode/triode configurations[6]. Measurements using electrostatic probes investigated the role of plasma oscillations in driving electron transport in the plume of a high current cathode operating a high-power MS HET on xenon[7]. This study provided algebraic closures for fluid models that can lead to better agreement with measurements. An additional study using electrostatic probes to measure a 20 A hollow cathode operating on argon indicated that exposure to HET-like magnetic fields can lead to unexpected oscillatory behavior, the physics of which were not well understood[8]. Internal emitter measurements using high-speed probes on a hollow cathode up to 10 A, along with electron microscopy and spectroscopy measurements, indicate that emitter failure modes and axial plasma property distributions (that also affect the orifice and plume plasmas) are dependent on emitter surface chemistry. These physics models require measurements for validation and calibration[9,10].

Simulations of 100 A class cathodes performed using OrCA2D showed no significant difference from a lower-current, geometrically-comparable cathode, namely the NSTAR cathode operating on xenon[11]. A kinetic, axisymmetric plasma simulation code was developed to study the cathode plume plasma for lifetime and performance predictions and tested against NSTAR cathode simulations and measurements[12]. Centerline data diverged from measurements when using the Boltzmann relation as a closure for the potential profile, indicating that unresolved physics, such as ion acoustic turbulence, was missing in the simulations. Improved 1D fluid insert plasma models[13] and hybrid-PIC plume models[14] indicated an under-prediction of the electron properties in the insert region and plume when compared to Langmuir probe measurements unless induced magnetic field and anomalous resistivity related to ion-acoustic turbulence were included in the simulations. This highlights the need for minimally invasive measurements at the relevant operating conditions in order to update models for simulations.

While laser induced fluorescence (LIF) can provide insight into ion behavior and coherent laser Thomson scattering (LTS) can provide direct density fluctuation information[15], near-field minimally invasive measurements of electron temperature and density are required to study the near-field physics of the electrons. Such electron properties can be determined using incoherent LTS. Recently, axially resolved incoherent LTS was applied to the near field plume of a 60 A class hollow cathode operating at 15 A on xenon in a small (1 m x 0.6 m) vacuum facility for electron Mach number studies[16]. The authors did not mention absolute number density calibration in this work, and therefore the number density detection limit cannot be determined.

With the end goal of studying the near-field discharge of high-power HETs, this paper outlines the implementation of an incoherent LTS system in a large vacuum test facility at the Georgia Tech High-Power Electric Propulsion Laboratory (HPEPL). The system is tested using a high-current hollow cathode as the plasma source. The general design of the LTS system leveraged previously implemented systems[16,17], with the goal of maximizing the solid angle through the collection optical system. These optimizations were achieved through the implementation of custom interrogation beam, collection, and detection optical systems while simultaneously reducing the number of degrees of freedom necessary for alignment. The performance of the system, quantified through the detection limit, is compared to other systems in the EP literature. Axially resolved electron temperature and density measurements are made from 2 to 8 mm of the cathode keeper face of a stand-alone cathode discharge with an external anode and no applied magnetic field operating at 25 A on krypton. The resulting profiles for the electron properties are compared to those found in the literature.

II. EXPERIMENTAL SETUP

A. Vacuum Test Facility

This experiment was conducted in Vacuum Test Facility 2 (VTF-2) at the Georgia Tech HPEPL. VTF-2 is a 4.9 m diameter and 9.2 m long stainless steel chamber. Its operation is described in Reference[18]. This system provides a combined xenon pumping speed of 350,000 l/s and achieves an ultimate base pressure of 1.9×10^{-9} Torr $-$ N_2.

The pressure in the facility, from the atmospheric pressure of ca. 760 Torr to a medium vacuum of 1 Torr, was monitored using a Kurt J Lesker XCG-BT-FB-1 capacitance manometer mounted on a flange at the periphery of the chamber. A capacitance manometer was chosen for its accuracy of $\pm 0.5\%$ and the fact that no gas-specific corrections are needed. The error in the calibrated manometer pressure output versus the expected local atmospheric pressure due to the horizontal mounting of the manometer was corrected by using a linear fit. The medium vacuum pressure, from 1 Torr to 1 mTorr, was measured using an Agilent Varian 531 Thermocouple Vacuum gauge mounted at the periphery of the facility on a flange.

The high vacuum pressures inside of the facility at less than 1 mTorr were measured at two locations via Agilent Bayard-Alpert 571 hot-filament ionization gauges. One was 0.5 m radially from the test section and the other was at the periphery of the facility mounted to a flange. The measured operational and base pressures were averaged over these two gauges and then the operational pressure was corrected for krypton via

$$p_{\mathrm{operational-corrected}} = \frac{1}{c_{\mathrm{corr}}} \left(p_{\mathrm{operational-measured}} - p_{\mathrm{base}}\right) + p_{\mathrm{base}}, \quad (1)$$

with c_{corr} being equal to 1.96 for krypton[19]. During the LTS acquisitions, the base and operational pressures in the facility were 2.55×10^{-7} Torr $-$ N_2 and 1.33×10^{-6} Torr $-$ Kr, respectively.

B. Cathode Discharge Configuration

The test article in this experiment was a 60 A lanthanum hexaboride (LaB_6) hollow cathode whose design heritage stems from the HERMeS and H6 HETs hollow cathodes, designed for use in the H9[3] and extrapolation into the X3 nested HET[20], referred to going forward as the H9 cathode. The target discharge current for this experiment was 25 A. An external stainless-steel cylindrical anode of length $L_{\text{anode}} = 211$ mm and diameter $D_{\text{anode}} = 302$ mm was placed 152 mm away from the H9 cathode keeper face and used to close the discharge circuit. The anode and cathode keeper were aligned coaxially. Figure 1 shows a schematic of the cathode discharge mounted in the facility.

Mass flow to the cathode was metered by an MKS GE40A mass flow controller (MFC) mounted externally to the facility. The controller was calibrated at the test section inside of VTF-2 using a MesaLabs DryCal 800-10 volumetric flow meter system, creating a linear fit between the desired flow rate and the measured flow rate in the test section.

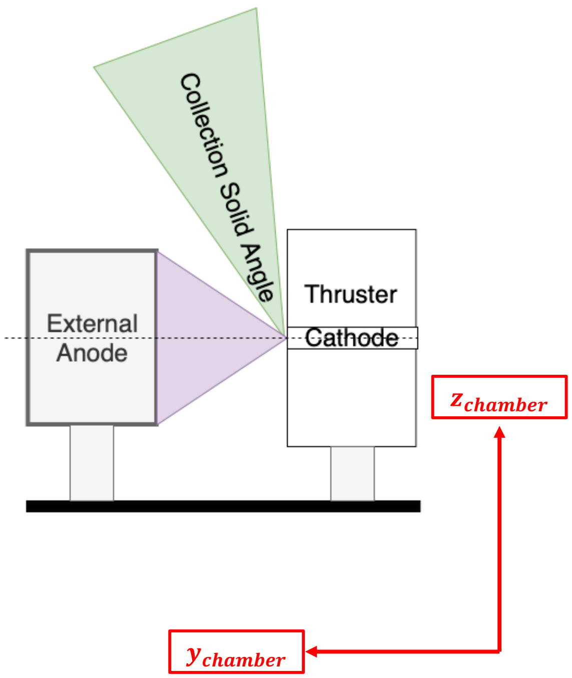

FIG. 1: Side-view diagram of the cathode discharge mounted inside of VTF-2. The external anode to cathode keeper face separation distance is 211 mm. The diameter of the external anode is 302 mm.

In order to spatially resolve the electron properties in the near-keeper plume of the H9 cathode, it is necessary to translate the cathode relative to the LTS beam and collection optics. This was accomplished by mounting the H9 cathode discharge assembly on motion stages. The Parker 4062000XR motion stages were configured in an $\mathbf{x}_{\text{chamber}} - \mathbf{y}_{\text{chamber}}$ configuration, with $\mathbf{z}_{\text{chamber}}$ oriented according to the right hand rule. Figure 2 shows the orientation of the motion stages, their positive travel direction, and the chamber axis definitions, as well as the interrogation, collection, and detection optical axes to be described in the next section. A Newport 281 manual lab jack was used to visually align the vertical positioning of the cathode such that the centerline of the cathode keeper orifice was coincident with the $\mathbf{z}_{\text{chamber}}$ position of the interrogation laser beam. The anode was also placed on an optical rail assembly, which allowed for easy alignment perpendicular to and along the axis coincident with the center axis of the cathode.

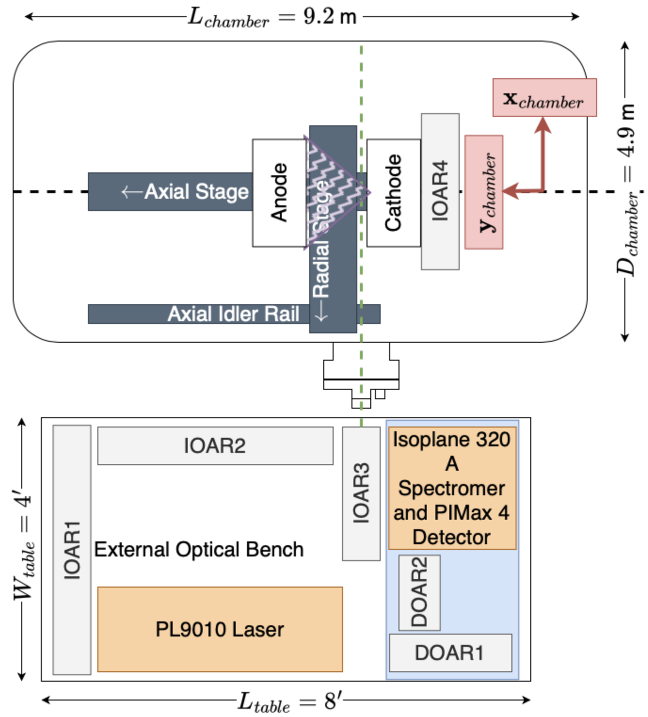

FIG. 2: Top-down diagram of the relative location of the external optical system with respect to the vacuum test facility. IOAR and DOAR area acronyms for interrogation optical axis rail and detection optical axis rail, respectively. Diagram not to scale.

C. Interrogation Beam Optics

Figure 2 outlines the relative positions between the VTF-2 facility and the major components for this experiment. The dashed line in green represents the optical axis of the interrogation beam, which is a chord through the center of the chamber cross-section, aligned perpendicular to the axial centerline of the chamber along $\mathbf{x}_{\text{chamber}}$. The structures inside of the chamber, including the thrust stand, are designed to facilitate HETs and other plasma sources being coaxial with this axial centerline of the chamber, parallel to $\mathbf{y}_{\text{chamber}}$.

Figure 3 shows a detailed schematic of the optical configuration and Table I outlines the optical components used. An Amplitude DLS Powerlite 9010 injection seeded Nd:YAG laser, operating at the second harmonic of 532 nm, provided a 9 mm diameter beam with a laser pulse duration between 5 and 8 ns and maximum energy of 1.15 J/pulse with an energy stability of better than 1% over a time period of ten minutes, as measured by a Gentec UP52N-50S-QED-D0 power meter, $I-PM_1$. Several beam blocking elements, like $I-PM_1$ and $I-BD_2$, are placed on flip mounts and only intermittently placed in the beam path as needed. To help guide the reader, the optical configuration downstream of the laser is divided into segments along each optical axis used in the interrogation (laser-to-test section), collection (test section-to-optical fiber), and detection (fiber-to-spectrometer) portions of the light path. Irises were used along the entire beam path to set, monitor, and maintain the alignment of the optical axes.

Interrogation optical axis rail 1 (IOAR1) began with a two-to-one beam expander ($I-l_1$ and $I-l_2$). Adjustment of this beam expander also allowed improved collimation along the entire optical path, which was several meters long. The beam expander was followed by a half-wave plate ($I-HWP_1$) and polarizing beamsplitter cube ($I-PBS_1$) to allow reduction of the interrogation beam power during alignment, while still operating the laser at its nominal conditions. On IOAR2, a second half-wave plate ($I-HWP_2$) was used to control the polarization of the laser beam within the chamber, allowing maximization of the LTS signal for the collection angle used in the chamber.

TABLE I: Interrogation Beam Optical Parameters

Element	**Aperture Size**	**Focal length**
Laser	-	-
$I-M_i$	50.8 mm	-
$I-BD_i$	20.0 mm	-
$I-PM_1$	20.0 mm	-
$I-i_i$	Variable	-
$I-HWP_i$	20.0 mm	-
$I-PBS_1$	25.4 mm	-
$I-l_1$	25.4 mm	-50 mm
$I-l_2$	25.4 mm	100 mm
$I-l_3$	25.4 mm	400 mm

Two mirrors ($I-M_3$ and $I-M_4$) brought the laser beam up to the height of the center axis of VTF-2, along IOAR3, whose long axis was parallel to $\mathbf{z}_{\text{chamber}}$. Micrometer-driven translation stages were used for the positioning of critical optical elements, such as $I-M_3$ and $I-M_4$. $I-M_4$ directed the beam along the final interrogation axis, IOAR4, into the vacuum chamber. A custom Torr Scientific NSQ1462-25 KF-flanged Brewster window was placed on the flange through which the beam passed in order to maximize energy throughput into the facility and minimize reflections. Additionally, all beam paths outside of the chamber (detection, interrogation) were enclosed to reduce unwanted scattering.

Figure 4 shows a photograph of the optical configuration inside the vacuum chamber. The optical elements for IOAR4 inside the vacuum chamber were mounted on a breadboard that was attached to the thrust stand. The final focusing lens, $I-l_3$, was positioned and aligned on IOAR4 to intersect the beam waist with the image of the fiber bundle on the beam plane, setting interrogation volume. The two-to-one beam expander and the focal length of $I-l_3$ being 400 mm resulted in an expected beam waist diameter of less than 100 μm.

D. Light Collection and Detection Systems

There were three main design goals for the collection and detection systems. The first was maximizing (within practical constraints) the collection numerical aperture, while maintaining spatial resolution better than 2 mm × 2 mm. The second was the ability to remotely adjust the alignment of the collection system relative to the interrogation beam after pumping down the chamber, due to relative movement of the external optics and chamber as the facility is compressed during pumpdown. The final goal was the ability to probe within approximately 1-2 mm from the face of the cathode without the cathode structure interfering with the solid angle subtended by the collection lenses.

Due to the size of the facility, a fiber bundle was used to relay the light from the internal collection system to the external detection and filtering system. For the sake of bookkeeping, in Figure 3, the fiber faces $C-F_i$, are referred to as part of the collection system. Two custom Thorlabs FG200LEA-FBUNDLE fiber bundles, each containing seven 200 μm FG200LEA multimode fibers, were connected in series to relay the light from inside to outside of the facility. The fibers were arranged in a linear array on one end of each bundle and fanned out individual fibers on the other end. The fibers were fed through the facility wall at the fanned ends using a custom SQS Fiber Optics HEM048727 4.5 in. CF flange. On the air side of the chamber, the second fiber bundle relayed the light to the detection system.

The 200 μm diameter fibers were chosen because they provided good spatial resolution, in theory down to 200 μm × 200 μm when only using a single fiber, while having a high numerical aperture (NA) of 0.22. A bundle of linearly arranged fibers was chosen because it provided the greatest light collection along the beam propagation direction without sacrificing spatial resolution in the perpendicular directions. Higher NA fiber with a larger diameter would have presented challenges with relay lens NA matching, spectrometer NA lens matching, Bragg notch filters (BNF) clear aperture throughput, and rejection ring image-to-fiber image overlap[21]. The collection fiber bundle face $C-F_1$ was mounted on a motorized translation stage with one rotational and three linear degrees of freedom, allowing adjustment of the fiber position and orientation to maximize signal collection after the facility was brought to vacuum.

Light from the measurement volume was relayed to the collection fiber bundle face, $C-F_1$, using a pair of 150 mm diameter, 350 mm focal length, NA = 0.210 lenses. Approximately 10% signal loss occurred due to the NA mismatch between the lenses and fibers. An AR-coated

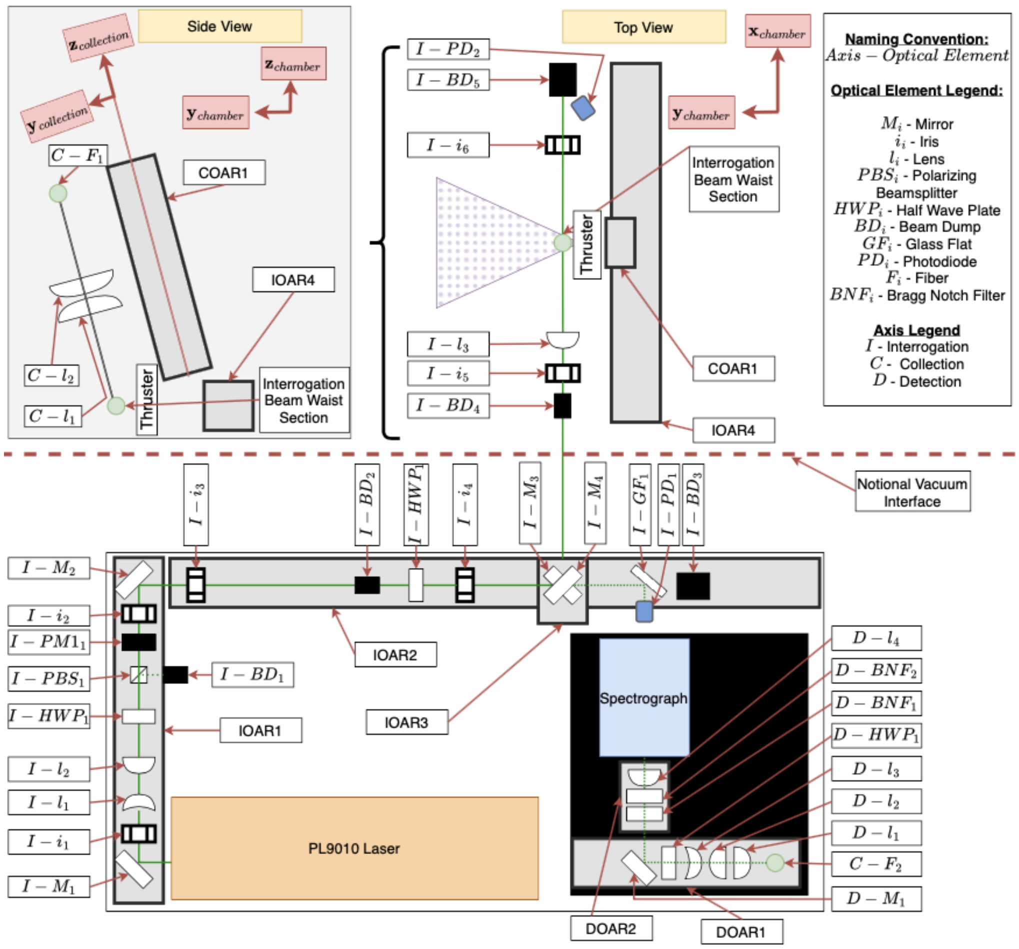

FIG. 3: Master optical diagram for the interrogation, collection and detection systems. $M, i, l, PBS, HWP, BD, PD, PM, F$ and BNF are acronyms for mirrors, irises, lenses, polarizing beamsplitter cubes, half wave plates, beam dumps, photodiodes, power meters, and Bragg notch filters, respectively. $I-$, $C-$ and $D-$ indicate interrogation, collection, and detection, the axes to which the optical element corresponds to, respectively.

glass flat was placed ahead of the first collecting lens in order to protect the lenses from deposits from the cathode, as well as allow for ease of cleaning without needing to completely realign the collection optical system.

The collection optical axis was tilted relative to z_{chamber}, as shown in Fig. 1. If the collection axis was aligned along the z_{chamber} direction, the cathode hardware would interfere with the angle subtended by the collection lenses, thus reducing the signal collected. Furthermore, this interference would change depending on the proximity of measurement volume to the cathode face, requiring different number-density calibrations at each position. In the angled configuration used, the measurement volume could be brought to the cathode face without interference between the cathode and the light collection solid angle. As mentioned previously, the polarization of the interrogation beam was rotated to maximize the signal along this axis.

The light transmitted to the end of the fiber bundle $C-F_2$ was processed, spectrally filtered through the two OptiGrate OD-4 BNFs, and then relayed into the spectrograph via the detection optical system. Two BNFs were used to extend the rejection region parallel to the length of the fiber bundle, see Ref.[21] for details to maximize light collection and effectively eliminate stray light. Figure 5 illustrates the optics used in the detection system and their ideal ray optics matrices used for design and optimization. Table II outlines the optics used and their relative distances. The spectrograph was comprised of a Princeton Instruments ISOPLANE-320A spectrometer and PM4-1024i-HB-FG-18-P46 PIMAX4 camera with gate width set to 12 ns.

As stated previously, the individual fiber NA is 0.22. However, the spectrograph had $f/\# = 4.6$, corresponding to a spectrometer acceptance angle that is about half of the emission angle of the fiber. Given this, it was impossible to satisfy the Helmholtz-Lagrange invariant while keeping the detection system magnification to less

PLEASE CITE THIS ARTICLE AS DOI: 10.1063/5.0180251

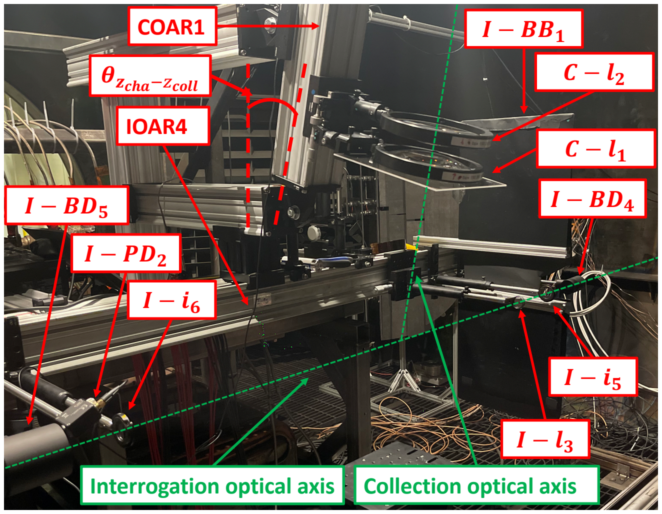

FIG. 4: A photo of the internal optical rail structure that supports the last leg of the interrogation optical axis and the collection optical axis. The green dashed lines show the path the laser beam will travel along IOAR4 along the interrogation optical axis, and the path the center of the scattered light follows along COAR1 along the collection optical axis. $I - BB_1$ is a set of Thorlabs beam blocks used to block reflections from the Brewster window to the interrogation section to help minimize stray light.

than two to minimize the required slit width opening and to ensure that the BNF rejection rings were able to completely overlap the fiber image on the spectrometer plane. Therefore, as described below, there was a non-negligible loss at the BNFs given their 15 mm aperture.

TABLE II: Detection System Optical Parameters

Element	D/ID (mm)	f/Distance (mm)
$\Delta z_{l_1/beam}$	-	100
l_1	50.8	100
$\Delta z_{l_2/l_1}$	-	25
l_2	50.8	200
$\Delta z_{l_3/l_2}$	-	150
l_3	25.4	-50
$\Delta z_{HWP_1/l_3}$	-	25
HWP_1	25.4	25
$\Delta z_{BNF_1/HWP_1}$	-	25
BNF_1	15	-
$\Delta z_{BNF_2/BNF_1}$	-	25
BNF_2	15	-
$\Delta z_{l_4/BNF_2}$	-	75
l_4	25.4	100
$\Delta z_{slit/l_4}$	-	-

The area ratio between the clear aperture of the BNF and the maximum ray height from the optical axis at the BNF is 0.634 for an effective fiber NA of .201. Therefore, the effective collection NA in this configuration is 0.133, an approximately 34% loss compared to 0.201, which leads to a usable collection solid angle ($\Delta\Omega$) of 0.055 sr, even with the losses due to the filters. In order to minimize losses due to vignetting, the optics between which the light was expected to be collimated were separated by no more than 25 mm, with particular care taken to minimize the distance $\Delta z_{\mathrm{BNF_1/l_3}}$. It is unclear in the literature at this time if the coupling out of the fiber systems through the detection optics on comparable systems deployed elsewhere have designed for the effect of the magnification on the light coupled into the spectrometer. The combination of magnification and image size of the fibers on the slit, the size of the rejection ring from the BNF on the image of the fibers on the slit plane, and the slit opening are crucial for optimizing the light throughput the detection stage of the optical path.

E. Fiber Alignment and Chamber Compression Movement Correction

The entire optical system was aligned prior to each intended testing campaign. However, the system became slightly misaligned during the pump-down process due to compression of the chamber. Any slight misalignment negatively affected the collection efficiency and, hence, a system was implemented to maintain the alignment during pumpdown and every hour during the acquisition of data. In order to minimize the number of degrees of freedom for alignment, instead of moving the fiber bundle and the collection lenses relative to each other and also relative to the interrogation beam, the fiber bundle was the only movable optical element from outside of the facility. Given the diameter of the fibers at 200 μm, and the diameter of the beam expected to be approximately 100 μm, the movement of the fibers needed to be in steps on the order of μm.

Several tests were performed to understand the adverse effects of the facility pumpdown on the optical system alignment. These tests indicated some very important points. First, the relative movement of the beam waist with respect to the collection optical axis is small even though the measured beam waist correction movement using a micrometer stage indicated that the chamber moved almost 5 mm. However, even though the beam incident on the lens moved approximately 5 mm, the focus moved less than 2 mm perpendicular to the incident laser beam propagation direction. Nevertheless, given the size of the beam and the fibers, this is non-negligible and must be accounted for. The second point is that the thrust stand optical rail structure is rigid and that the mounting of the optics on this structure ensured no relative movement of anything on the structure. Additionally, the vibration of the roughing pump system is not the dominant factor in the uncertainty in the signal intensity when collecting LRS data. This was determined from signal collected at atmosphere when the roughing systems from both VTF facilities in the building were

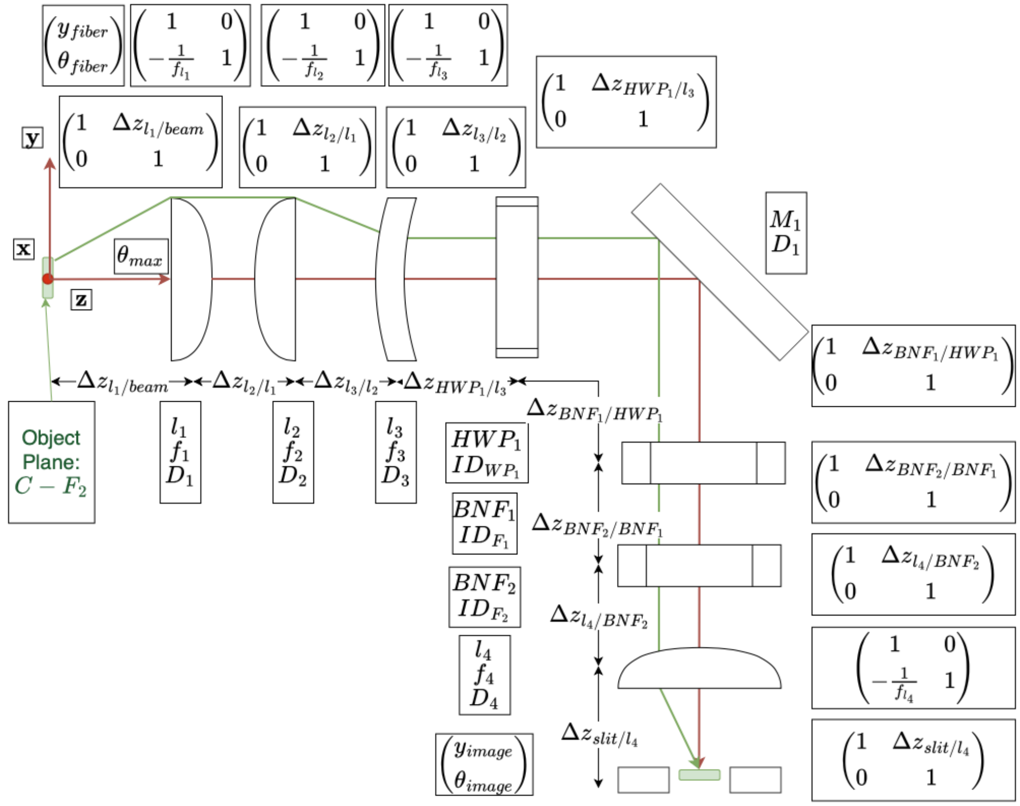

FIG. 5: Detection system optical diagram. The optical elements, their relative spacing, their individual ray matrices, and their relative spacing ray matrices are labeled. The optimized detection parameters are outlined in Table II

active.

Each fiber movement direction had a different level of sensitivity. The $\mathbf{x}_{\text{collection}}$ axis did not have a strong sensitivity because the observed beam waist was $\mathcal{O}(10\text{ mm})$ along the $\mathbf{x}_{\text{collection}}$ direction.The movement of the fiber parallel to $\mathbf{z}_{\text{collection}}$ was expected to be sensitive on the order of mm. This was not observed during this iteration of the optical setup. As stated, there is a loss of about 34% at the BNFs and about 10% due to the NA of the lenses. As a result, the system appears to be less sensitive with movements parallel to $\mathbf{z}_{\text{collection}}$ because the rays that would be lost due to this sensitivity are the ones that are being cut off by the BNFs; the solution to this that preserves the Helmholtz-Lagrange invariant is to add larger BNF filters to the system. The system is extremely sensitive in $\mathbf{y}_{\text{collection}}$, which is the direction that effectively overlaps the fiber image with the interrogation beam. Micron-level adjustments were necessary for proper optimization/coupling of the fiber image and beam in the $\mathbf{y}_{\text{collection}}$ direction. This is critical, as the signal increased almost 10-fold when properly coupled compared to when it is improperly coupled by displacements of greater than the width of the beam waist, about 100 μm.

Given the results of the aforementioned test, the movement of the interrogation beam relative to the inner structure was corrected in the following way. Firstly, before pumpdown, the targets $I-i_5$ and $I-i_6$ were closed so as to barely clip the beam but not cause significant reflections, and used as targets from outside of the facility for coarse beam readjustment using $I-M_3$ and $I-M_4$. Then, the $\mathbf{y}_{\text{collection}}$ translation stage was optimized in order to maximize the signal. This was done for every pressure at which Raman measurements (described below) were made for the absolute number density calibration. This procedure ensured the alignment was always optimized at all pressures. The chamber was observed to compress approximately 5 mm axially from 760 to 10 Torr. After this, the chamber movement was negligible with respect to the movement on the iris. However, micrometer level changes needed to be made using the fiber motion stages.

III. SCATTERING OF ELECTROMAGNETIC RADIATION

Incident radiation interacts with matter, accelerating the charges in the matter, which leads to the re-radiation, consistent with the differential scattering cross-section of the matter for the scattering process of interest. Scattered power intensity is directional, and the characteristics of the scattered radiation are dependent on the reference frame and direction of observation, all of which are wrapped into the differential scattering cross-section.

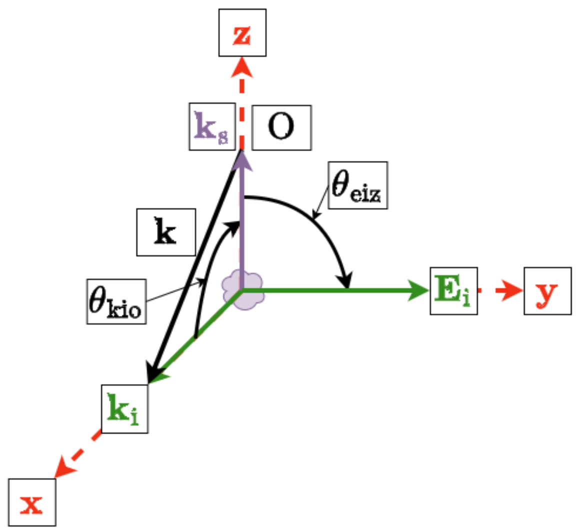

FIG. 6: General scattering wave vector orientations in a scattering experiment. The basis vectors $\mathbf{x}, \mathbf{y}, \mathbf{z}$ are mutually perpendicular. The vectors $\mathbf{k}_\mathrm{i}$ and $\mathbf{k}_\mathrm{s}$ and $\mathbf{k} \equiv \mathbf{k}_\mathrm{i} - \mathbf{k}_\mathrm{s}$ are coplaner, with the angle between $\mathbf{k}_\mathrm{i}$ and $\mathbf{k}_\mathrm{s}$, θ_kio all being in the $\mathbf{x}-\mathbf{z}$ plane. $\mathbf{E}_\mathrm{i}$ is in the $\mathbf{x}-\mathbf{y}$ plane along with the angle θ_eiz. In the experiment detailed above, $\theta_\mathrm{kio} = \pi/2$ and θ_eiz=0, axis $\mathbf{z}$ is parallel to COAR1. The angle from $\mathbf{z}_\mathrm{chamber}$ to $\mathbf{z}$ is $\theta_{\mathbf{z}_\mathrm{cha}-\mathbf{z}_{coll}} = 15°$.Given that $\mathbf{z}_\mathrm{chamber}$ is parallel to the exit plane of the thruster, making the angle between the collection axis $\mathbf{z}$ and the face of the thruster 15°. This can be seen in Figure 7.

Figure 6 depicts the scattering configuration with all relevant angles and vector orientations that appear in the description of our scattering model equations in sections sections III A and III B.

We are interested in the spectrally-distributed total scattered power per pulse/shot of incident radiation, averaged over an accumulation of shots. For detailed derivations, see Refs.[22–27]. The general equation representing the spectrally distributed total scattering signal in units of counts per nm is

$$P_\lambda = \underbrace{\underbrace{\underbrace{\eta \frac{\lambda_\mathrm{i}}{hc} \Delta\Omega\, L\, E_\mathrm{i}}_{\mathrm{I}}\, n \frac{\partial\sigma}{\partial\Omega}(\lambda)}_{\mathrm{II}}\, S(\lambda)}_{\mathrm{III}}, \tag{2}$$

where η is the intensified photoelectron to scattered photon calibration constant, λ_i is the incident wavelength, h is the Planck constant, c is the speed of light, $\Delta\Omega$ is the solid angle of collection, L is the length of the probe volume, E_i is incident laser energy, n is the scatterer number density, $\partial\sigma/\partial\Omega$ is the scattering cross section per unit solid angle, and S is the spectral redistribution function. λ_i/hc gives the photons per joule at the incident wavelength. The braces denote (I) the leading constants that are often grouped as "system calibration constant", C_sys; (II) the magnitude of the scattered power, and (III) the total scattered power, which is redistributed spectrally due to broadening mechanisms. The differential scattering cross section per unit solid angle contains all of the physics of the scattering of interest. The wavelength dependence of the scattering cross section and spectral distribution function is explicitly stated in Equation 2, but is omitted in the rest for compactness. We discuss the relevant rotational Raman and Thomson scattering in the following subsections.

A. Rotational Raman Scattering

Laser rotational Raman scattering (LRS) is necessary in order to calibrate the absolute electron number density measurements in an LTS experiment. LRS is the inelastic scattering of incident radiation from polyatomic molecules as the result of a net exchange of energy from the incident radiation and the internal energy modes of the molecule[22,23]. For a diatomic molecule, its rotational selection rules for the possible transitions in the rotational quantum number J follow $J' = J \rightarrow J \pm 2$ for Stokes (+) and anti-Stokes (-) transitions, respectively.[28,29]. It can be shown (see Refs.[22,30]) that the rotational Raman scattering cross section is the sum of the Stokes and anti-Stokes cross sections as

$$\frac{\partial\sigma^\mathrm{R}}{\partial\Omega} = \sum_J \frac{\partial\sigma^\mathrm{R}}{\partial\Omega}_\mathrm{Stokes} + \sum_J \frac{\partial\sigma^\mathrm{R}}{\partial\Omega}_\mathrm{anti\text{-}Stokes}. \tag{3}$$

The Stokes and anti-Stokes cross sections, $\frac{\partial\sigma}{\partial\Omega}_{J'}$, relate the perpendicular scattering cross sections $\frac{\partial\sigma}{\partial\Omega}^\perp_{J'}$, to the population faction $\frac{n_J}{n_\mathrm{g}}$, through

$$\frac{\partial\sigma}{\partial\Omega}_{J'} = \frac{n_J}{n_\mathrm{g}} \left\{(1-\rho)\cos^2(\zeta)\left[1-\cos^2(\theta_\mathrm{kio})\sin^2(\theta_\mathrm{eiz})\right] + \rho\right\} \frac{\partial\sigma}{\partial\Omega}^\perp_{J'}. \tag{4}$$

In Equation 4, ρ, ζ, θ_kio, and θ_eiz being the depolarization ratio, the angle between the polarization of the scattered Raman radiation and the incident radiation, the angle between the incident radiation propagation direction and the direction of scattering observation, and the angle between the incident radiations polarization and the $\mathbf{z}$ axis, in Figure 6, respectively.

The ratio of the Jth population level (n_J) to the total number density of particles (n_g) is quantified through the partition function as

$$\frac{n_J}{n_\mathrm{g}} = \frac{1}{Q_\mathrm{g}} g_J (2J+1) \exp\left[-\frac{\epsilon_J(J)}{k_\mathrm{B}T_\mathrm{g}}\right]. \tag{5}$$

The perpendicular Raman cross section, $(\partial\sigma/\partial\Omega)^{\perp}_{J'}$, is

$$\frac{\partial\sigma}{\partial\Omega}^{\perp}_{J'} = \frac{64\pi^4}{45}\frac{\gamma^2}{\epsilon_{\mathrm{o}}^2}\frac{b_{J'}}{\lambda_{J'}^4}, \tag{6}$$

with g_J being the nuclear spin degeneracy and depends on whether the value of J is even or odd. For nitrogen, g_{J} is equal to 3 and 6 when J is odd or even, respectively. Similarly, for oxygen, g_{J} is equal to 1 and 0 when J is odd or even, respectively.

The anisotropy of the molecular polarizability tensor, $\gamma^2/\epsilon_{\mathrm{o}}^2$, is linearly interpolated from experimental measurements at the frequency of interest, as is typical in Refs.[30–32]. The rotational energy mode, rotational partition function, ideal gas law, Placzek-Teller coefficients, and Raman scattering wavelengths are

$$\epsilon_J(J) = hc\left[B_{\mathrm{g}}J\,(J+1) - D_{\mathrm{g}}J^2\,(J+1)^2\right], \tag{7}$$

$$Q_{\mathrm{g}} = \frac{(2I_{\mathrm{g}}+1)^2\,k_{\mathrm{B}}\,T_{\mathrm{g}}}{2B_{\mathrm{g}}hc}, \tag{8}$$

$$p_{\mathrm{g}} = n_{\mathrm{g}}\,k_{\mathrm{B}}\,T_{\mathrm{g}}, \tag{9}$$

$$b_{J'}(J) = \frac{3}{8}\frac{(2J+1\pm1)(2J+1\pm3)}{(2J+1)(2J+1\pm2)}, \tag{10}$$

and

$$\lambda_{J'}(J) = \lambda_{\mathrm{i}} \pm \lambda_{\mathrm{i}}^2 B_{\mathrm{g}}(4J+2\pm4), \tag{11}$$

respectively. B_{g} and D_{g} are the molecular rotation constant and centrifugal distortion constants, respectively, and they both depend on the gas species. $B_{\mathrm{g}} = 199$ m^{-1} for nitrogen and 143.8 m^{-1} for oxygen. $D_{\mathrm{g}} = 5.7\times10^{-4}$ m^{-1} for nitrogen and 4.8×10^{-4} m^{-1} for oxygen. T_{g} and k_{b} are the equilibrium scattering gas temperature and Boltzmann constant.

In the case of rotational Raman scattering, we assume the only relevant source of spectral redistribution is due to the finite detection optics, spectrometer, and detection system – commonly referred to as the instrument function – because Doppler and pressure broadening are negligible. We assume that this (integral normalized) function can be modeled by a Gaussian probability density function, resulting in a spectral redistribution function

$$S^{\mathrm{R}}(\lambda_{J'},\lambda_{\mathrm{i}},\tau) = \frac{1}{\sqrt{2\pi}\sigma_{\mathrm{if}}(\tau)}\exp\left[-\frac{1}{2}\left(\frac{\lambda_{\mathrm{i}}-\lambda_{J'}}{\sigma_{\mathrm{if}}(\tau)}\right)^2\right]. \tag{12}$$

Traditionally, instrument functions are described with full-width half maximums (FWHM), τ. Here, τ is one of the parameters fit using least squares to the LRS spectrum (see below) and is not independently measured. We can relate this to the Gaussian instrument function width σ_{if} via

$$\sigma_{\mathrm{if}}(\tau) = \frac{\tau}{2\sqrt{2\log(2)}}. \tag{13}$$

In the Raman case, given that we model this as the only source of broadening, the redistribution operation becomes a simple convolution. However, given that each Raman transition produces a single intensity at the particular Raman wavelength, we are mathematically convolving a Gaussian with a Dirac delta function at each transition. As such, the convolution is simply the peak intensity of the Raman line multiplied by the instrument function Gaussian centered at that Raman transition wavelength. Hence, we can explicitly state the expected Raman signal, in photon counts per nm, for a single species indexed by χ_j, as

$$P_\lambda^{\mathrm{R}}|_{\chi_j} = \eta\frac{\lambda_{\mathrm{i}}}{hc}\,\Delta\Omega\,L\,E_{\mathrm{i}}\,n_{\chi_j}(T,p_{\chi_j})\left[\sum_J\frac{\partial\sigma^{\mathrm{R}}}{\partial\Omega}_{J'}\right]_{\chi_j} S_\lambda^{\mathrm{R}}(\lambda_{J'},\tau)\,, \tag{14}$$

For the case of air (modeled as a two-component mixture of N_2 and O_2),

$$P_\lambda^{\mathrm{R}}(\mathbf{x}^{\mathrm{R}},\boldsymbol{\theta}^{\mathrm{R}}) = \eta\frac{\lambda_{\mathrm{i}}}{hc}\,\Delta\Omega\,L\,E_{\mathrm{i}}\,n_{\mathrm{g}}(T_{\mathrm{g}},p_{\mathrm{g}})\left[\gamma_{\mathrm{N_2}}\left[\sum_J\frac{\partial\sigma^{\mathrm{R}}}{\partial\Omega}_{J'}\right]_{N_2} + \gamma_{\mathrm{O_2}}\left[\sum_J\frac{\partial\sigma^{\mathrm{R}}}{\partial\Omega}_{J'}\right]_{O_2}\right] S_\lambda^{\mathrm{R}}(\lambda_{J'},\tau)\,, \tag{15}$$

with $\gamma_{\mathrm{N_2}} = .79$ and $\gamma_{\mathrm{O_2}} = 0.21$.

Here, we explicitly call out the dependencies of P_λ^{R} on the quantities of interest (QoI) in our calibration measurements ($\mathbf{x}^{\mathrm{R}}$) and so-called nuisance parameters (θ^{R}) that influence the scattered power but are not of primary interest to the measurement, via

$$\mathbf{x}^{\mathrm{R}} = [T_{\mathrm{g}},\tau,\eta,\lambda_{\mathrm{i}}]^\top\,,\ \theta^{\mathrm{R}} = p_{\mathrm{g}}. \tag{16}$$

In this formulation, the neutral gas temperature is estimated from the fit to the data using the width of the LRS spectrum, the FWHM is fit with respect to the width of the LRS linewidths, the efficiency constant is fit to the amplitude of the LRS spectrum and the data, and finally, the center wavelength is fit with respect to the center of the spectrum.

B. Incoherent Thomson Scattering

LTS is the elastic electromagnetic scattering of incident radiation from unbounded charged particles and can be coherent or incoherent. Sections 2.2 and 2.4 in Refs.[31,32], respectively, discuss the cases in which the experimental setup and plasma conditions meet the conditions for coherent Thomson scattering. In short, the type of scatter generated and detected is largely determined by the physical construction of the interrogation beam path and the collection system[33] as well as the Salpeter parameter, $\alpha_{\mathrm{salp}} = 1/k\lambda_{\mathrm{D}}$, with λ_{D} being the electron Debye length[32]. When the Salpeter parameter is less than one, incoherent effects dominate. For a $n_{\mathrm{e}} = 1 \times 10^{17}$ m^{-3} and $T_{\mathrm{e}} = 10$ eV, the Salpeter parameter is approximately .05, squarely in the incoherent regime. Therefore, in this work, we consider only incoherent LTS. The expected electron density and temperature ranges of $1 \times 10^{17} - 1 \times 10^{18}$ m^{-3} and $1 - 10$ eV, as well as the single interrogation laser beam, were expected to produce scattering in the incoherent regime.

For LTS, the wavelengths of the scattered radiation are consistent with the Doppler shifted motion of the individual electrons along the scattering wave vector $\mathbf{k}$; see Chapters 1 and 4 of Ref.[26] and Chapter 2 of Ref.[31] for details. It can be shown that the electron Thomson scattering cross section is

$$\frac{\partial \sigma^{\mathrm{T}}}{\partial \Omega} = r_{\mathrm{e}}^2 \left[1 - \cos^2(\theta_{\mathrm{kio}}) \sin^2(\theta_{\mathrm{eiz}})\right], \qquad (17)$$

with the classical electron radius being $r_{\mathrm{e}} = 2.82 \times 10^{-15}$ m. For LTS, the redistribution of the total scattered power is dominated by two wavelength shifts caused by the relative motion of each scattering electron with respect to the observer of the scatter[26]. This is directly linked to the relative velocity of the observer and the scattering electron along the scattering wave vector, $\mathbf{k} \equiv \mathbf{k}_{\mathrm{i}} - \mathbf{k}_{\mathrm{s}}$, with $\mathbf{k}_{\mathrm{i}}$ being the incident propagation wave vector and $\mathbf{k}_{\mathrm{s}}$ being the wave vector along the direction from the scattering volume to the observer. To avoid confusion, the spectral distribution function is explicitly labeled with k to indicate that it is along the direction of the scattering wave vector, in whatever unit vector basis is used to define these vectors.

For an ensemble of electrons, the spectral distribution shape function is directly related to the electron velocity distribution function (EVDF) along the scattering wave vector, f_{k}. The scattering redistribution happens over tens of nm, an order of magnitude or greater than that of the instrument function broadening, justifying why that contribution to the broadening is often neglected, as is done here. Given this, the total scattered power is redistributed over the spectral band dictated by the EVDF along the scattering wave vector. For a plasma whose electron population is in thermal equilibrium, the spectral distribution function $S_{\mathrm{k}}(\lambda)$ corresponds to a Maxwellian EVDF that can be related to the equilibrium electron temperature T_{e}; the classical electron temperature is the full descriptor for the shape of the distribution in such plasmas[31,34]. There are several analytical models that can be applied for non-equilibrium plasmas, including bi-Maxwellian and Druyvesteyn distributions[35–38]. For robust plasma model selection using Bayesian inference, please see Suazo Betancourt et al.[39] Here, we evaluate our LTS signals in the context of pure Maxwellian plasmas.

In general for LTS,

$$P_{\lambda}^{\mathrm{T}}\left(\mathbf{x}^{\mathrm{T}}, \boldsymbol{\theta}^{\mathrm{T}}\right) = \eta \frac{\lambda_{\mathrm{i}}}{hc} \Delta\Omega\, L\, E_{\mathrm{i}}\, n_{\mathrm{e}} \frac{\partial \sigma^{\mathrm{T}}}{\partial \Omega} S_{\mathrm{k},\lambda}^{\mathrm{T}}\left(\mathbf{x}^{\mathrm{T}}, \lambda_i\right). \qquad (18)$$

This function is parameterized by the QoI and nuisance parameter vectors,

$$\mathbf{x}^{\mathrm{T}} = [T_{\mathrm{e}}, n_{\mathrm{e}}, v_{\mathrm{d}}]^{\top} \quad \text{, and } \boldsymbol{\theta}^{\mathrm{T}} = \quad [\eta, \lambda_{\mathrm{i}}]^{\top}. \qquad (19)$$

with v_{d} being the magnitude of the bulk drift velocity along the scattering wave vector. Please note that, the scattering wave vector is not guaranteed to be parallel to any basis vector of interest in your system. In our case, the scattering wave vector has a component parallel to the thruster axial axis, and one parallel to the cathode (and therefore thruster) radial vector given that we are probing along the cathode centerline. These vectors are detailed in Figure 6. For reconciliation between the scattering wave vector and the thruster axis vectors, see Reference[40]. The least squares fitting of v_{d} is equivalent to finding the center of the shifted LTS spectrum. This is equivalent to the method in Equation 3.13 of Reference[31] because it is explicitly included in Equation 20.

For a Maxwellian plasma, the spectral distribution function is[31]

$$S_{\mathrm{k},\omega}^{\mathrm{TM}} = \frac{1}{\sqrt{2\pi}} \frac{1}{k_{\sigma}\sigma_{\mathrm{T}}} \exp\left[-\frac{1}{2}\left(\frac{\omega_{\mathrm{i}} - \omega - k_{\sigma} v_{\mathrm{d}}}{k_{\sigma}\sigma_{\mathrm{T}}}\right)^2\right]. \qquad (20)$$

In this case, the scattered power can be sub-scripted to specify a Maxwellian spectral distribution function as $P_{\lambda}^{\mathrm{TM}}\left(\mathbf{x}^{\mathrm{TM}}\right)$). The incident and scattered frequencies, the magnitude of the scattering wave vector, and σ_{T} are represented by

$$\omega_{\mathrm{i}} = \frac{2\pi c}{n_{\mathrm{R}}} \frac{1}{\lambda_{\mathrm{i}}}, \omega = \frac{2\pi c}{n_{\mathrm{R}}} \frac{1}{\lambda}, \qquad (21)$$

$$k_{\mathrm{i}} = \frac{2\pi}{\omega_{\mathrm{i}}}, k = \frac{2\pi}{\omega}, \qquad (22)$$

$$k_{\sigma} = \sqrt{k_{\mathrm{i}}^2 + k^2 - 2k_{\mathrm{i}}k\cos\theta_{\mathrm{kio}}} \approx 2k_{\mathrm{i}} \sin\left(\frac{\theta_{\mathrm{kio}}}{2}\right), \qquad (23)$$

and

$$\sigma_{\mathrm{T}} \equiv \sqrt{\frac{k_{\mathrm{B}} T_{\mathrm{e}}}{m_{\mathrm{e}}}}. \qquad (24)$$

In these equations, n_{R} is the refractive index (not to be confused with previous uses of n for number density) and m_{e} is the electron mass.

Finally, the distribution above is presented in the frequency ω domain. It is necessary to convert these to wavelength, which is achieved via

$$\frac{\partial \omega}{\partial \lambda} = \frac{2\pi c}{n_{\mathrm{R}}} \frac{1}{\lambda^2}, \tag{25}$$

such that

$$S_{\mathrm{k},\lambda}(\lambda) = \frac{\partial \omega}{\partial \lambda} S_{\mathrm{k},\omega}(\omega(\lambda)). \tag{26}$$

C. Data Preprocessing and Uncertainty

The LRS and LTS models presented produce an intensity at each wavelength λ. A spectrum of collected data can be represented using a vector,

$$\mathbf{b} = \left[P_{\lambda_1}, P_{\lambda_2}, \ldots, P_{\lambda_{N_\lambda}}\right]^\top, \tag{27}$$

where N_λ is the number of spectrally resolved measurements. It is oftentimes necessary to reject parts of a spectrum straddling the laser wavelength. The truncated spectrum is $\mathbf{b}|_{\mathrm{trunc}}$, with the rejected wavelength range being bounded between $\lambda^{\mathrm{rej}}_{\mathrm{min}}$ and $\lambda^{\mathrm{rej}}_{\mathrm{max}}$. The rejection regions were taken as a constant multiple of the inferred FWHM, 4τ. This arbitrary choice was made to automate this process and tuned to work across multiple datasets under analysis at the time.

In our case, we collect LTS scattered light from plasmas that are created by ionizing krypton, which is a monatomic species. Our detection system is calibrated by collecting LRS from the air, taken as a mixture of diatomic N_2 and O_2. The relay from the face of the fiber, as the only source of light reaching the detection leg of the system, effectively eliminated the influence of reflections on the collected signal; there was negligible parasitic stray light. As a result, in the LRS case, a background correction with the laser off was sufficient to recover an invertible LRS spectrum. For the same reason as the LRS case, a background subtraction by the plasma emission spectrum with the laser off was sufficient to recover an invertible LTS spectrum.

A least squares (LS) inversion of the pre-processed signals was implemented in Python and used to determine the parameter vectors of interest and their variance in accordance with a 95% confidence interval procedure[41]. This procedure involves solving for the QoI, $\mathbf{x}$, and then using the residuals between the model functions and the signal to estimate the covariance matrix for the QoI variables. The variance in the measured facility pressure was less than 1%, and was therefore not added to the uncertainty in η via uncertainty propagation. In the Raman case, this procedure is applied at each neutral gas pressure after background subtraction and normalizing the collected signals by the number of total accumulations. The neutral gas pressure and incident laser energy are variables in the LRS model, and the incident laser energy is a variable in the LTS model. The spectra were not pressure or energy normalized, but instead, those measured parameters were passed into the models directly. An alternative method is to plot the signal intensity as a function of pressure, the slope of this curve being related to η through Equation 15. This method relates the uncertainty to the line fit using R^2 as opposed to ascribing individual uncertainties based on the SNR of the spectra and was therefore not used in this work. Then, λ_{i} and η are used as constants for the LTS LS signal inversion. Using comparison with Bayesian analysis, Suazo Betancourt et al.[39] showed that LS inversion provides representative uncertainty bounds, even when the uncertainties in λ_{i} and η are not explicitly included via uncertainty propagation for the final values of $\mathbf{x}^{\mathrm{T}}$ and $\delta\mathbf{x}^{\mathrm{T}}$. This is only true in the case where the variance between the calculated efficiency constant between pressures is less than 10%. However, as will be detailed in the next section, because the variance between mean values of η was more than 10%, uncertainty propagation was necessary for representative error bars on the electron number density. The final uncertainty in the electron number density was calculated according to

$$\delta n_{\mathrm{e}}|_{\mathrm{max}} = n_{\mathrm{e}} \sqrt{\left(\frac{\delta n_{\mathrm{e}}}{n_{\mathrm{e}}}\right)^2 + \left(\frac{\Delta\eta|_{\mathrm{max}}}{\bar{\eta}}\right)^2}. \tag{28}$$

In this equation, $\delta n_{\mathrm{e}}|_{\mathrm{max}}$ is the η variance corrected number density variance, δn_{e} is the least squares residual based variance on the number density. The value of δn_{e} is calculated after estimating the covariance matrix from the residuals of the least squares fit[41]. $\Delta\eta|_{\mathrm{max}}$ is the maximum difference between the mean calculated values of η, and $\bar{\eta}$ is the ensemble mean value of η. As stated previously, the drift velocity v_{d} is included in Equation 20, and is fitted at a given value of λ_{i} and its uncertainty is calculated using the least squares residuals. However, the uncertainty in mean values of λ_{i} leads to uncertainty in the drift velocity as well. We choose to represent this as a rejection region in v_{d} space. We calculate the mean value over all pressures, $\bar{\lambda}_{\mathrm{i}}$, and use this as the center wavelength and take the uncertainty as the difference between the minimum and maximum value λ_{i} overall pressures as $\Delta\lambda_{\mathrm{i}}|_{\mathrm{max}}$. $\bar{\lambda}_{\mathrm{i}} \pm \Delta\lambda_{\mathrm{i}}|_{\mathrm{max}}$ is then converted to a drift velocity range using $\omega_{\mathrm{i}} - \omega_{\mathrm{c}} = k_\sigma v_{\mathrm{d}}$ from Equation 20. In the case where $\Delta\lambda_{\mathrm{i}}|_{\mathrm{max}}$ is less than the spectrometer resolution per pixel, the spectrometer resolution sets the drift velocity by setting $\Delta\lambda_{\mathrm{i}}|_{\mathrm{max}}$ to the spectrometer resolution

IV. RESULTS AND DISCUSSION

The cathode discharge was operated at 25 A and 60 V, with a flow rate through the cathode of 1.79 mg/s of krypton. Axial profiles were taken from 2 mm to 8 mm in 1 mm steps from the face of the cathode along the centerline and at 2 mm radially from the centerline. The positioning of the interrogation beam relative to the cathode is shown in Fig. 7. The incident laser propagation is parallel to $\mathbf{x}_{\text{collection}}$, and the collection axis is $\mathbf{y}_{\text{collection}}$ is shifted $\theta_{\mathbf{z}_{\text{cha}}-\mathbf{z}_{coll}} = 15°$ forward with respect to the face of the HET, the drift velocity is pointed 45° clockwise from the thruster midplane and 15° out from the plane of the thruster face. The incident laser energy, E_{i} was 194 mJ/pulse during the LTS acquisitions and variable during the LRS acquisitions and described below. The detection system parameters for all subsequent tests were the same. The detector was set to a gate width of 12 ns with a gain of 100 and a spectrum was a single frame with 3000 accumulations. The spectrometer used a 2400 l/mm, leading to a wavelength resolution of .0283 nm/pixel. The slit parallel to the fibers was set to 5 mm, and the slit perpendicular to the fiber was set to 450 μm. This allowed for a full capture of the interrogation volume defined by the fiber in the chamber, accounting for the system magnification of two.

A. LRS Calibration Results

Several Raman calibration points were taken with air in the facility at pressures of 105, 50.6, 26.4, 13.0, and 5.60 Torr-Air at laser energies of 121, 121, 200, 207, and 207 mJ/pulse, respectively. LRS was collected at a minimum pressure of 5 Torr due to LRS SNR being limited in the current configuration. Changes to the interrogation optical axis to maximize incident laser energy and detector-binning would allow for collection of LRS as low as possibly 5 mTorr. The incident laser energy was limited to 200 mJ/pulse due to ionization effects observed during LRS calibration; a shift from an LRS spectrum to a clearly LTS spectrum due to ionization was observed at higher pulse energies. This was due to the combination of upstream beam expansion and the minimization of the focal length of $I - l_3$.

Figure 8 presents two sample LRS spectra. The center wavelength and optical system collection efficiency at each pressure are presented in Figure 9. There is an approximately 15% variance in the calculated calibration constants between pressures. This is due to small changes in the fiber location relative to the beam and laser energy fluctuations. The overlap of the fiber image with respect to the beam happens over a ± 100 μm distance. However, various effects – from slight changes in the thermal state of the laser to the vacuum test facility settling into a given position at a new pressure over the acquisition – can lead to slight misalignments. A later experiment that intentionally misaligned the fiber image on the beam waist plane saw a decrease of up to 50% in the efficiency constant. Over all pressures, the ensemble mean and standard deviation between mean values of η and λ_{i} were $\eta = 0.185 \pm .027$ (15%) and $\lambda_{\text{i}} = 532.07 \pm .046$ (0.05%) nm, respectively. However, at each pressure, the variance on η and λ_{i} are less than 10% and 1%, respectively.

B. Cathode LTS Results

Figure 10 presents two sample LTS spectra, after background subtraction, at the maximum number density position and the minimum number density above the system detection limit (described below). The result of the fit to the Maxwellian plasma spectral distribution also is shown in the figure. The center wavelength of the spectrum, λ_{c}, is distinguished from the incident wavelength calculated from the Raman inversion, λ_{i}, showing the ability to distinguish between a spectrum that is shifted from the incident wavelength due to the bulk drift velocity. At the minimum and maximum number density positions, the mean values of λ_{c} are 532.096 and 531.885 nm, respectively, which correspond to mean drift velocity values of 9 km/s and -60.4 km/s, respectively.

These data demonstrate that simple background subtraction, without wavelength binning or smoothing, recovers invertible signals with reasonable SNR. We define the detection limits of our system as corresponding to peak-signal to mean-noise ratio of one, which was found to occur at number densities of approximately 1×10^{17} m^{-3}. Figure 11 shows the spatial distribution of the parameters of interest, demonstrating the uncertainty in derived plasma properties at the detection limit defined above.

C. Quantitative Comparison with Similar LTS Systems

The inversion and uncertainty based on the signal fits indicate that the system design goals of good signal generation, collection, and throughput were accomplished. The implemented diagnostic acquired signal above the stated detection limit with the least number of accumulations and minimum laser energy compared to similar systems to date[16,17].

Achieving this SNR and detection limit was in large part due to the minimization of the interrogation focal length. This minimized the beam waist size to match the size of the fiber image on the interrogation beam plane. Additionally, the two large diameter collection lens system and the four-lens detection optical system both that were designed to maximize light collection and transmission through the system. We can quantitatively compare our system to those found in References[16,17] through the effective solid angle, detection length, and incident laser energy. Our inner chamber collection system has $E_{\text{i}} L_{\text{det}} \Delta\Omega = 44.1$ mm sr mJ pulse^{-1} at an incident laser energy of 195 mJ/pulse and spatial resolution of 100 μm × 1.4 mm, given that the beam waist is approx 100 µm. The system has a number density detection limit of $1{\times}10^{17}$ m^{-3}, maximum expected electron temperature

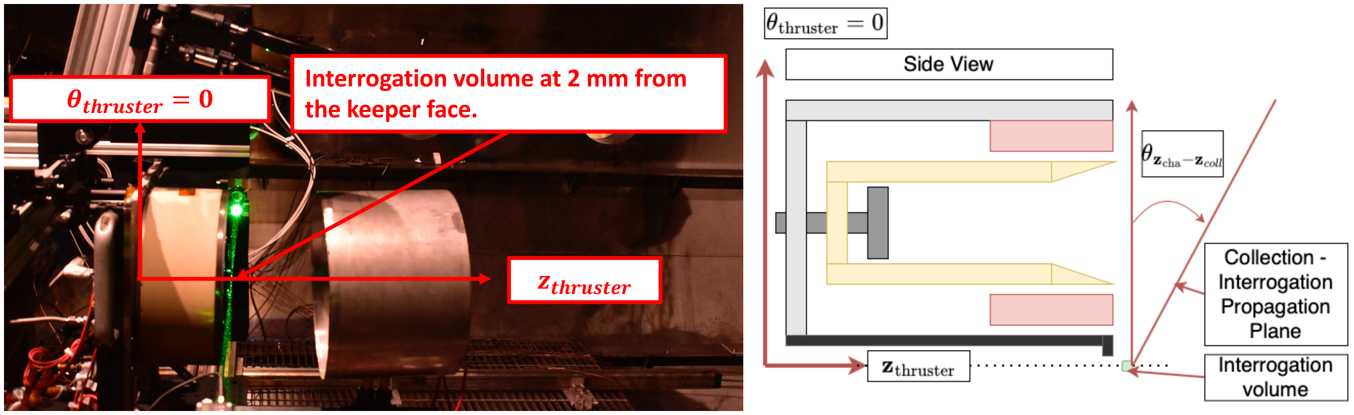

FIG. 7: Image of the final configuration of the interrogation and collection system at atmospheric chamber pressure along with a figure of the relative location of the interrogation volume relative to the thruster $\mathbf{z}_{\text{thruster}} - \theta_{\text{thruster}}$ axes. $\mathbf{z}_{\text{thruster}} - \theta_{\text{thruster}}$ is aligned with the thruster axis of symmetry, shown by the dotted line.

at this limit of 15-20 eV, and minimum drift velocity of 10 kms^{-1}.

Accounting for magnification in Reference[17,31], the effective $E_{\text{i}} L_{\text{det}} \Delta\Omega$ is 31 mm sr mJ pulse^{-1}, with a spatial resolution of .825 μm $\times$.495 μm. The authors reported a number density detection limit of $1{\times}10^{16}$ m^{-3} and maximum detectable temperature at this limit of approximately 50 eV[40], and drift velocity limits of 500 kms^{-1}.

The system in Reference[16] has an effective $E_{\text{i}} L_{\text{det}} \Delta\Omega$ of 40.8 mm sr mJ pulse^{-1} with a spatial resolution of 200 μm$\times$200 μm. These calculations do not account for area ratios of collimated rays passing through the filtering elements or conservation of the Helmholtz-Lagrange invariant given the lack of information in Reference[16] necessary to calculate these properties. However, the maximum temperature and minimum drift velocity measured were 12 eV and 600 kms^{-1}. More recent measurements lead to the expected density, temperature and drift velocity limits to be approximately $1{\times}10^{17}$ m^{-3}, 80 eV, and 5 kms^{-1}. The difference in effective throughput of the systems, the stated detection limits, and the capital spectroscopic equipment (e.g, the spectrometer and detector) highlight the need for standardization of the basic equations and pre/post-processing used across LTS teams against a well documented and known test-set of data.

We expect that future measurements at even more challenging conditions, e.g. at least one order of magnitude lower number densities in the near field plume of HETs, will be possible by increasing the number of laser shots accumulated and incident laser energy, and modifying the beam expansion ratio, the interrogation beam focal length, and changing the acquisition strategy in order to use leverage vertical pixel and horizontal pixel / wavelength binning. Specifically, a reduction in $I - l_1$ to a focal length of 75 mm and increasing $I - l_3$ to a focal length of 600 mm will allow us to increase our incident laser energy to the full output capacity of the laser, 1000 mJ/pulse. Vertical on-detector binning over the entire range of pixels illuminated by the fiber image on the slit plane will reduce read noise by approximately a factor of 10. This will minimize noise on the detector and increase the scattering signal intensity to increase the total SNR and, therefore, decrease the detection limit to an expected 2×10^{16} m^{-3}. Additionally, the radial variations seen in Figure 11 necessitate increasing spatial resolution by averaging over fewer fibers with the hardware-based binning. In the current configuration, the spatial resolution can be increased to 200 μm $\times$ 200 μm

D. Qualitative and Quantitative Comparison of the Electron Property Profiles

Based on the relative size and location of our anode and cathode, the neutral pressure downstream of the cathode exit in our experiment is expected to be 1-2 orders of magnitude lower than those often reported in the literature[2,42,43]. This aligns with the 1-2 orders of magnitude lower electron number density presented in Fig. 11 compared to the these previously reported cathode discharge experiments and simulations[2,42,43]. The electron number density decreases by approximately an order of magnitude from 2 mm to 8 mm along the cathode centerline as seen in Figure 11. The shape of the centerline axial profile (at $\mathbf{r}_{\text{beam}-\text{cathode}} = 0$) is consistent with the previous data[15], showing a sharp drop-off in the electron number density that asymptotically approaches the background electron density. The increasing electron temperature is consistent with LIF, as well as coherent[44?] and incoherent LTS[16,45] measurements that indicate increasing ion temperatures as the plasma expands toward the anode .

The electron temperature and density axial profiles at $\mathbf{r}_{\text{beam}-\text{cathode}} = 2$ mm are consistent with a core plume plasma expanding between our cathode and anode, superimposed on a background plasma, with the core plasma bounded by the angle between the cathode

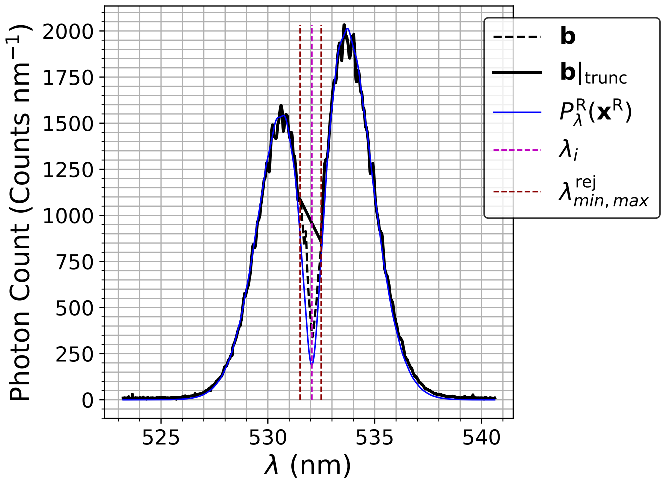

(a)

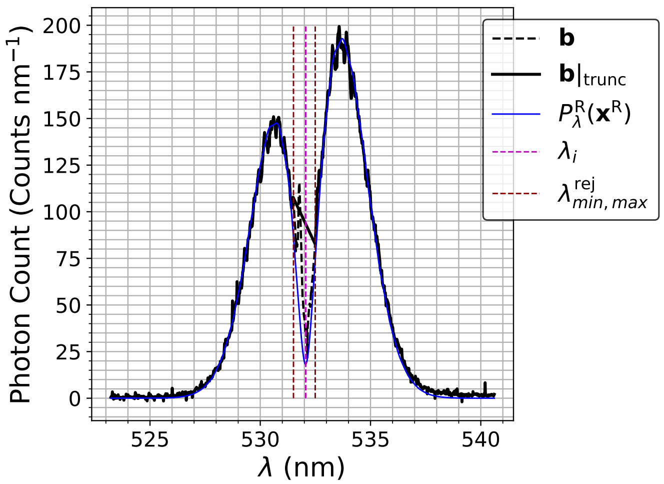

(b)

FIG. 8: Least squares fitted spectra for the rotational Raman inversion; (a) and (b) show the raw and truncated ($\mathbf{b}$ and $\mathbf{b}|_{\text{trunc}}$) with rejection regions and model spectra ($P_\lambda^{\text{R}}\left(\mathbf{x}^{\text{R}}\right)$) at 105 Torr and 5.6 Torr, respectively. The corresponding neutral gas temperature estimated at both pressures is 272 K and 268 K with uncertainties of less than 1%.

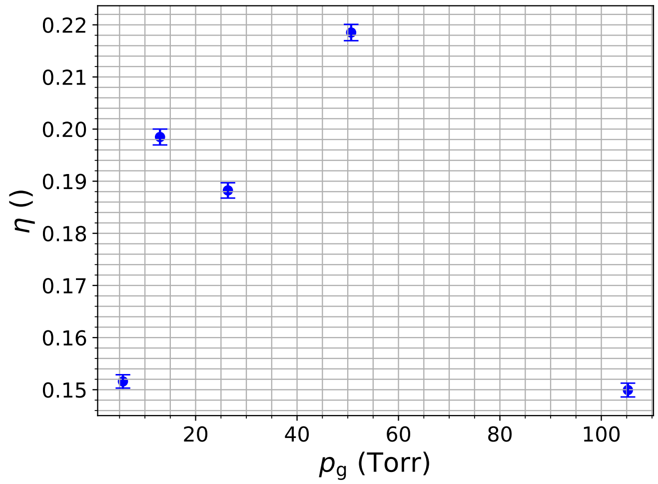

(a)

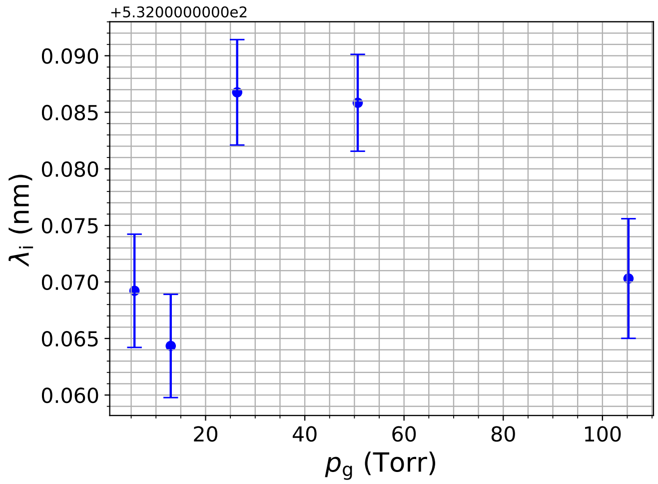

(b)

FIG. 9: Least squares fitted quantities of interest for the rotational Raman inversion; (a) shows system efficiency constant versus background pressure and (b) shows estimated center wavelength versus background pressure. Note that the wavelength axis is centered around 532 nm.

orifice plate and the external anode. The plasma expansion is diagrammed in Figure 1. The bulk of the plasma is expected to be confined to within this angle. The expanding plasma electrons are thought to be interacting with the background neutrals, which are expected to be of significant density in the region close to the cathode[43], and sustaining a spatially uniform background plasma near the edges of the expanding core plasma between the cathode and the anode. Alternatively, the data could suggest that this region of plasma just outside of the expanding plasma jet is driven by charge exchange due to the approximately constant electron number density up until $z = 5$ mm, which then rapidly decays at a rate consistent with that along the center line. However, this is unlikely since the charge exchange mean free path in a facility of this size is expected to be on the order of meters.

The electron bulk velocity profiles, both along the centerline and at a radius of 2 mm, indicate acceleration along the positive scattering wave vector up to axial positions of 4-6 mm, followed by deceleration to a negative velocity from 5 to 8 mm. The orientation of the scattering wave vector being almost perpendicular to the cathode axial axis is expected to be the reason for the low drift velocity on the order of tens of kms^{-1}. The

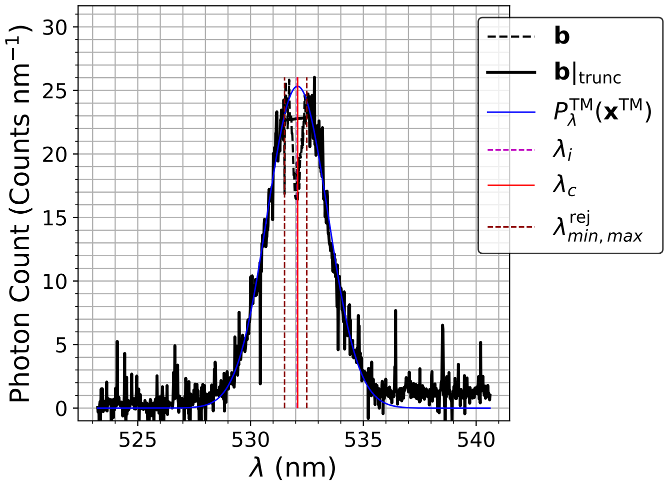

(a)

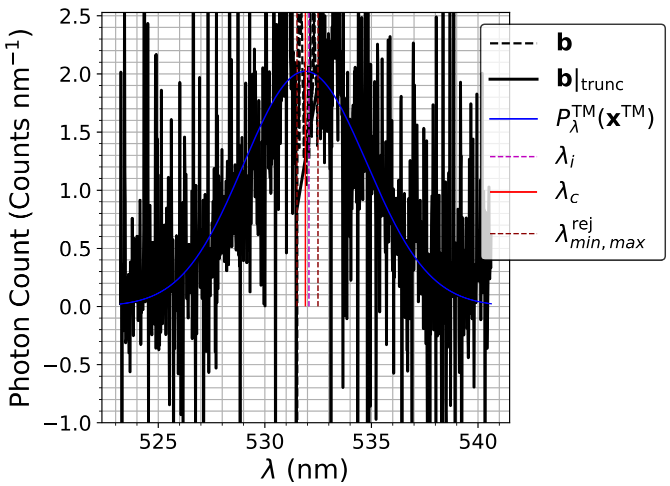

(b)

FIG. 10: Least squares fitted results for the laser Thomson scattering inversion; (a) and (b) show the raw and truncated ($\mathbf{b}$ and $\mathbf{b}|_{\text{trunc}}$) model spectra for a Maxwellian ($P_\lambda^{\text{TM}}\left(\mathbf{x}^{\text{TM}}\right)$) spectral distribution function. Figures (a) and (b) correspond to absolute number densities of $\mathbf{1.07 \times 10^{18}}$ and $\mathbf{1.85 \times 10^{17}}$ m^{-3}, and electron temperatures of 1.65 and 7.81 V eV, respectively. Figures (a) and (b) were taken along the center line at $\mathbf{z}_{\text{beam-cathode}}$ = 2 mm and $\mathbf{z}_{\text{beam-cathode}}$ = 8 mm, respectively. Figures (a) and (b) correspond to peak-signal to mean-noise ratios of 14.3 and 1.81, respectively.

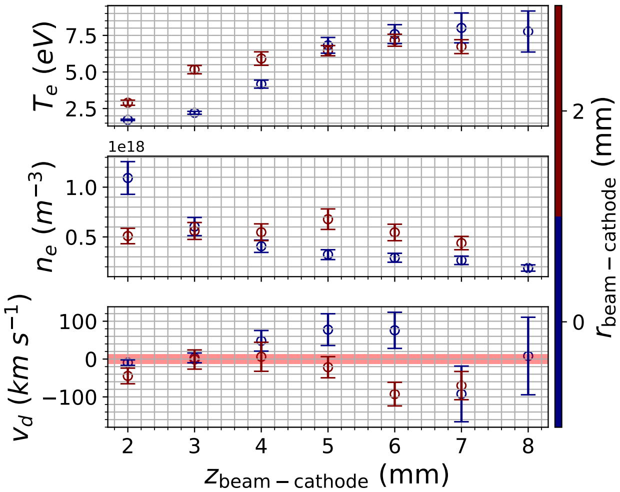

(a)

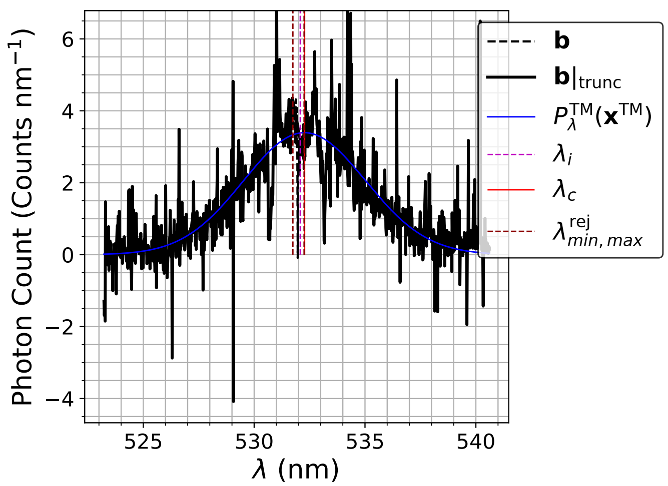

(b)

FIG. 11: (a) Axially resolved electron properties calculated using Maxwellian spectral distribution submodel at two different radii (b) LTS spectrum at 5 mm showing the maximum drift velocity via the clear offset between λ_c and λ_i. In (a) The centerline data is in blue and the data at a radius of 2 mm from the cathode keeper centerline is in red. At a radius of $\mathbf{r}_{\text{beam-cathode}}$ = 2 mm, the signal at $\mathbf{z}_{\text{beam-cathode}}$ = 8 mm was very low and, as a result was not included. The rejection region, shown in red in (a), in drift velocity space is described in the last paragraph of III.C.

bulk drift velocity unit vector and the maximum expansion angle (defined by the relative size and distance of the cathode and anode) are different by thirty degrees. In order for the cathode electrons to make contact with the anode after expanding, they need to accelerate towards the anode, which necessitates a component along the negative scattering wave unit vector. This measured bulk velocity profiles indicate a plasma plume expanding from the plasma orifice in a manner similar to a nozzle, which is then redirected towards the anode through a standing electrostatic potential between the cathode and anode. Full three-component resolution of the plasma bulk velocity with respect to the chamber or thruster basis vectors would require several investigations with an orientation change of the signal collection branch. When applied to the thruster, a simpler option for resolving the bulk velocity components is outlined in Reference[40].

V. CONCLUSIONS

A laser Thomson scattering system was implemented in a large-scale vacuum test facility. The diagnostic was used to take axially resolved electron density and temperature measurements of a cathode discharge with an external anode. A mechanical structure inside of the facility allowed for the degrees of freedom necessary to orient the collection and interrogation beam propagation to allow for LTS collection up to the face of the cathode keeper. The internal optical structure also allowed for the placement of the interrogation beam focusing lens inside the facility. This minimized its distance to the thruster, maximizing the collected scatter through the beam waist diameter less than or equal to in size than the image of the fibers on the beam plane. Additionally, the internal single optical degree of freedom through the movement of only the fiber face relative to pre-defined collection optical axes and lenses allowed for easy alignment correction to the true optimum alignment from outside of the facility using a simple set of targets and a single set of motion stages. The mechanical and optical layout described is adaptable to other large VTF facilities. This system allowed for relatively high SNR data to be acquired with minimal laser energy and accumulations, allowing for implementation using smaller, more compact lasers. Methods for maximizing the SNR in this configuration are discussed in the previous section. The data collected provides a path forward for measurements of the electron temperature and density in the near field of high-power HET discharges. The number density and temperature data collected corroborates previous measurements in this region, with the expected rapid decay in number density having been observed. Discrepancies in the magnitude of the electron density have been attributed to the size and placement of the discharge anode. This may be cause for a standardization of the relative position and size of discharge anodes in stand-alone cathode experiments for easier comparison across measurements and measurement comparison to plasma simulations.

[1] R. G. Jahn, *Physics of Electric Propulsion* (Dover Publications, 2006) pp. 1–50.

[2] D. M. Goebel and I. Katz, *Fundamentals of Electric Propulsion: Ion and Hall Thrusters* (Wiley, 2008).

[3] R. R. Hofer, S. E. Cusson, R. B. Lobbia, and A. D. Gallimore, "The H9 Magnetically Shielded Hall Thruster," in *35th International Electric Propulsion Conference, Atlanta, GA* (2017).

[4] D. M. Goebel and E. Chu, "High-Current Lanthanum Hexaboride Hollow Cathode for High-Power Hall Thrusters," Journal of Propulsion and Power **30**, 35–40 (2014).

[5] D. M. Goebel and J. E. Polk, "Lanthanum hexaboride hollow cathode for the asteroid redirect robotic mission 12.5 kW Hall thruster," in *Joint 30th ISTS, 34th IEPC and 6th NSAT Conf., Hyogo-Kobe, Japan, 4–10 July 2015* (2015).

[6] G.-C. Potrivitu, L. Xu, I. Levchenko, S. Huang, Y. Sun, M. Rohaizat, J. W. M. Lim, K. Bazaka, and S. Xu, "Mode transition in a low-current LaB6 hollow cathode for electric propulsion systems for small satellites," in *36th International Electric Propulsion Conference University of Vienna Austria* (2019).

[7] B. A. Jorns, S. E. Cusson, Z. Brown, and E. Dale, "Non-classical electron transport in the cathode plume of a Hall effect thruster," Physics of Plasmas **27**, 022311 (2020).

[8] Margaret Mooney and Kristina Lemmer, "Wave characterization of a hollow cathode plume in a HET- like magnetic field," in *37th International Electric Propulsion Conference Massachusetts Institute of Technology, Cambridge, MA USA* (2022).

[9] Gary Wan and Richard E. Wirz, "Surface Analysis of a High-Power LaB6 Hollow Cathode," in *37th International Electric Propulsion Conference Massachusetts Institute of Technology, Cambridge, MA USA* (2022).

[10] Yuya Oshio, Hiroki Watanabe, and Ikkoh Funaki, "Temperature and plasma measurement around the emitter region of the hollow cathode," in *37th International Electric Propulsion Conference Massachusetts Institute of Technology, Cambridge, MA USA* (2022).

[11] I. G. Mikellides, D. M. Goebel, B. A. Jorns, J. E. Polk, and P. Guerrero, "Numerical simulations of the partially ionized gas in a 100-A LaB6 hollow cathode," IEEE Transactions on Plasma Science **43** (2015), 10.1109/TPS.2014.2320876.

[12] A. R. Vazsonyi and I. D. Boyd, "An axisymmetric direct kinetic solver for simulation of hollow cathode plasmas," in *36th International Electric Propulsion Conference University of Vienna Austria* (2019).

[13] X. Chen, J. Navarro-Cavallé, and E. Ahedo, "Fluid Model of a Hollow Cathode Discharge," 36th International Electric Propulsion Conference University of Vienna Austria (2019).

[14] K. Kubota, Y. Oshio, K. Torii, Y. Okuno, H. Watanabe, S. Cho, I. Funaki, and G.-C. Potrivitu, "Comparisons between Hybrid-PIC Simulation and Plume Plasma Measurements of LaB6 Hollow Cathode," in *36th International Electric Propulsion Conference University of Vienna Austria* (2019).

[15] B. A. Jorns, C. Dodson, D. M. Goebel, and R. Wirz, "Propagation of ion acoustic wave energy in the plume of a high-current LaB6 hollow cathode," Physical Review E **96** (2017), 10.1103/PhysRevE.96.023208.

[16] P. J. Roberts and B. Jorns, "Characterization of Electron Mach Number in a Hollow Cathode with Thomson Scattering," in *AIAA SCITECH 2023 Forum* (American Institute of Aeronautics and Astronautics, Reston, Virginia, 2023) pp. 1–1.

[17] B. Vincent, S. Tsikata, S. Mazouffre, T. Minea, and J. Fils, "A compact new incoherent Thomson scattering diagnostic for low-temperature plasma studies," Plasma sources science & technology **27**, 55002 (2018).

[18] A. W. Kieckhafer and M. L. R. Walker, "Recirculating Liquid Nitrogen System for Operation of Cryogenic Pumps," in *32nd International Electric Propulsion Conference, Wiesbaden Germany* (2011).

[19] Saul Dushman, *Scientific Foundations of Vacuum Technique*, Vol. 4 (John Wiley & Sons, 1958).

[20] S. J. Hall, R. E. Florenz, A. Gallimore, H. Kamhawi, D. L. Brown, J. E. Polk, D. M. Goebel, and R. R. Hofer, "Implementation and Initial Validation of a 100-kW Class Nested-channel Hall Thruster," in *50th AIAA/ASME/SAE/ASEE Joint Propulsion Conference* (American Institute of Aeronautics and Astronautics, Reston, Virginia, 2014).

[21] J. Bak, J. L. Suazo Betancourt, A. Rekhy, A. Abbasszadehrad, R. B. Miles, C. M. Limbach, and M. L. R. Walker, "High resolution spatially extended 1D laser scattering diagnostics using volume Bragg grating notch filters," Review of Scientific Instruments **94**, 023003 (2023).

[22] Derek A. Long, "Classical Theory of Rayleigh and Raman Scattering," in *The Raman Effect* (John Wiley & Sons, Ltd, Chichester, UK, 2002) pp. 31–48.

[23] N. John and S. George, "Raman spectroscopy," in *Spectroscopic methods for nanomaterials characterization* (Elsevier, 2017) pp. 95–127.

[24] John David Jackson, "Classical Electrodynamics, Wiley," in *Classical Electrodynamics* (1998) 3rd ed., pp. 661–698.
[25] J. B. Marion and M. A. Heald, "Classical Electromagnetic Radiation," (1995).
[26] D. H. Froula, S. H. Glenzer, N. C. Luhmann, and J. Sheffield, "Scattered Power Spectrum," in *Plasma Scattering of Electromagnetic Radiation* (Elsevier, 2011) pp. 31–44.
[27] D. J. Griffiths, "Introduction to Electrodynamics," (American Association of Physics Teachers, 2005).
[28] David W. Ball, "The Basics of Spectroscopy,SPIE," in *The Basics of Spectroscopy* (2001) pp. 91–104.
[29] M. Hollas, "Modern Spectroscopy," in *Modern Spectroscopy* (2004) 4th ed., pp. 103–135.
[30] C. M. Penney, R. L. St. Peters, and M. Lapp, "Absolute rotational Raman cross sections for N_2, O_2, and CO_2," Journal of the Optical Society of America (1930) **64**, 712 (1974).
[31] B. Vincent, *Incoherent Thomson scattering investigations in Hall thruster, planar magnetron and ECR ion source plasmas*, Ph.D. thesis, ICARE - Institut de Combustion, Aérothermique, Réactivité et Environnement, Orleans (2019).
[32] M. J. van de Sande, *Laser scattering on low-temperature plasmas: High resolution and stray light rejection*, Ph.D. thesis, Eindhoven Technical University (2004).
[33] S. Tsikata and T. Minea, "Modulated Electron Cyclotron Drift Instability in a High-Power Pulsed Magnetron Discharge," Physical Review Letters **114**, 185001 (2015).
[34] W. G. Vincenti, C. H. Kruger, and T. Teichmann, " Introduction to Physical Gas Dynamics ," Physics Today **19** (1966), 10.1063/1.3047788.
[35] H. Sugai, I. Ghanashev, M. Hosokawa, K. Mizuno, K. Nakamura, H. Toyoda, and K. Yamauchi, "Electron energy distribution functions and the influence on fluorocarbon plasma chemistry," Plasma Sources Science and Technology **10**, 378–385 (2001).
[36] S. F. Adams, J. A. Miles, and V. I. Demidov, "Non-Maxwellian electron energy distribution function in a pulsed plasma modeled with dual effective temperatures," Physics of Plasmas **24**, 053508 (2017).
[37] A. A. Haji Abolhassani and J.-P. Matte, "Multi-temperature representation of electron velocity distribution functions. I. Fits to numerical results," Physics of Plasmas **19**, 102103 (2012).
[38] H. Amemiya, "Sheath Formation Criterion and Ion Flux for Non-Maxwellian Plasma," Journal of the Physical Society of Japan **66**, 1335–1338 (1997).
[39] Jean Luis Suazo Betancourt, Samuel J. Grauer, Junhwi Bak, Adam M. Steinberg, and Mitchell L. R. Walker, "Bayesian Model Selection For Thomson Scattering," Review of Scientific Instruments (2023).
[40] B. Vincent, S. Tsikata, and S. Mazouffre, "Incoherent Thomson scattering measurements of electron properties in a conventional and magnetically-shielded Hall thruster," Plasma sources science & technology **29**, 35015 (2020).
[41] G. A. F. Seber and C. J. Wild, "Nonlinear Regression," in *New Jersey: John Wiley & Sons*, Vol. 62 (2003) pp. 21–30.
[42] I. G. Mikellides and I. Katz, "Numerical simulations of Hall-effect plasma accelerators on a magnetic-field-aligned mesh," Physical Review E - Statistical, Nonlinear, and Soft Matter Physics **86** (2012), 10.1103/PhysRevE.86.046703.
[43] S. J. Hall, T. G. Gray, J. T. Yim, M. Choi, M. M. Mooney, T. R. Sarver-Verhey, and H. Kamhawi, "The effect of anode position on operation of a 25-A class hollow cathode," in *36th International Electric Propulsion Conference University of Vienna Austria*, GRC-E-DAA-TN72893 (2019) pp. 1–1.
[44] Sedina Tsikata, Thibault Dubois, and Kentaro Tara, "Coexistence of small-scale instabilities in Hall thrusters and hollow cathodes," in *37th International Electric Propulsion Conference Massachusetts Institute of Technology, Cambridge, MA USA* (2022).
[45] P. J. Roberts, B. A. Jorns, and V. H. Chaplin, "Experimental Characterization of Wave-Induced Azimuthal Ion Velocities in a Hollow Cathode Plume," in *AIAA SCITECH 2022 Forum* (American Institute of Aeronautics and Astronautics, Reston, Virginia, 2022).